Symmetry energy and the isoscaling properties of the fragments produced in ^{40}Ar,^{40} Ca+^{58}Fe,^{58} Ni reactions at 25, 33, 45, and 53 MeV/nucleon

J. Iglio, D.V. Shetty,* S. J. Yennello, G. A. Souliotis, M. Jandel, A. L. Keksis, S. N. Soisson, B. C. Stein, and S. Wuenschel
Cyclotron Institute, Texas A&M University, College Station, Texas 77843, USA

A. S. Botvina
Institute for Nuclear Research, Russian Academy of Science, RU-117312 Moscow, Russia
(Received 7 December 2005; published 24 August 2006)

The symmetry energy and the isoscaling properties of the fragments produced in the multifragmentation of ^{40}Ar,^{40} Ca+^{58}Fe,^{58} Ni reactions at 25, 33, 45, and 53 MeV/nucleon were investigated within the framework of statistical multifragmentation model. The isoscaling parameters α, from the primary (hot) and secondary (cold) fragment yield distributions, were studied as a function of excitation energy, isospin (neutron-to-proton asymmetry), and fragment symmetry energy. It is observed that the isoscaling parameter α decreases with increasing excitation energy and decreasing symmetry energy. The parameter α is also observed to increase with increasing difference in the isospin of the fragmenting system. The sequential decay of the primary fragments into secondary fragments, when studied as a function of excitation energy and isospin of the fragmenting system, show very little influence on the isoscaling parameter. The symmetry energy, however, has a strong influence on the isospin properties of the hot fragments. The experimentally observed scaling parameters can be explained by symmetry energy that is significantly lower than that for the ground-state nuclei near saturation density. The results indicate that the properties of hot nuclei at excitation energies, densities, and isospin away from the normal ground-state nuclei could be significantly different.

DOI: 10.1103/PhysRevC.74.024605 PACS number(s): 25.70.Mn, 25.70.Pq, 26.50.+x

I. INTRODUCTION

Recently the possibility of extracting information on the symmetry energy and the isospin (neutron-to-proton ratio) of the fragments in a multifragmentation reaction has gained tremendous importance [1–5]. Such information is of importance for understanding some of the key problems in astrophysics [4,6–12] and various aspects of nuclear physics, such as the structure of exotic nuclei (the binding energy and rms radii) [13–16] and the dynamics of heavy-ion collisions [17–24]. Traditionally, the symmetry energy of nuclei has been extracted by fitting the binding energy in their ground state with various versions of the liquid drop mass formula [28]. The properties of nuclear matter are then determined by theoretically extrapolating the nuclear models designed to study the structure of real nuclei. However, real nuclei are cold, nearly symmetric ($N \approx Z$) and found at equilibrium density. It is not known how the symmetry energy behaves at temperatures, isospin (neutron-to-proton ratio), and densities away from the normal nuclear matter. Theoretical many-body calculations [29–32] and those from the empirical liquid drop mass formula [33,34] predict symmetry energy near normal nuclear density ($\approx 0.17\,\mathrm{fm}^{-3}$) and temperature ($T \approx 0$ MeV) to be around 28–32 MeV.

In a multifragmentation reaction, an excited nucleus expands to a subnuclear density and disintegrates into various light and heavy fragments [35–38]. The fragments are highly excited and neutron rich; their yields depend on the available free energy that in turn depends on the strength of the symmetry energy and the extent to which the fragments expand. By studying the isotopic yield distribution of these fragments, one can extract important information about the symmetry energy and the properties of the fragments at densities, excitation energies, and isospin away from those of ground-state nuclei.

Experimentally, the determination of fragment isotopic yield distribution is not straightforward. It is influenced by the complex deexcitation of the hot (primary) fragments into observed cold (secondary) fragments. Theoretical calculations of the secondary deexcitations require accurate accounting of the feeding from the particle unstable states and are subject to uncertainties in the levels that can be excited and the structure effects that govern their decay [39–41].

From various statistical model approaches [5,25], it has been shown that the ratio of primary fragment yield for a given isotope or isotone produced in two different reactions with similar temperature, exhibit an exponential dependence on proton and neutron number, an observation known as isoscaling. The dependence has been interpreted in terms of a scaling parameter that is related to the symmetry energy of the primary fragment binding energy. The scaling parameter has been shown to be independent of the complex nature of the secondary deexcitation and is thus a robust observable for studying the fragment isotopic yield distribution.

In a recent work [1], it was shown that the symmetry energy of the primary fragments deduced from the reduced neutron density is significantly lower than that for the normal nuclei at saturation density. Le Fevre *et al.* [2], in their recent work studied the fragmentation of excited target residues following collisions of ^{12}C on ^{112,124}Sn at incident energies of

*Electronic address: shetty@comp.tamu.edu

300 and 600 MeV/nucleon. They observed that the symmetry energy coefficient deduced from the data are near 25 MeV for peripheral collisions and lower than 15 MeV for the central collisions. Henzlova *et al.* [3], studied the fragments produced in the multifragmentation of ^{136,124}Xe projectiles in midperipheral collisions with a lead target at 1 GeV/nucleon. They used both the $\langle N\rangle/Z$ ratio and the isoscaling of the fragments and found that the experimentally determined value of the scaling parameter can be reproduced within the statistical model framework by lowering the symmetry energy to as low as 11–12 MeV. However, the $\langle N\rangle/Z$ ratios of the fragments could be reproduced with symmetry energy coefficient as low as 14–15 MeV.

In this work, we study the primary fragment yield distribution in a number of reactions at various excitation energies and isospins using the isoscaling approach and the equilibrium statistical multifragmentation model. It is observed that the isoscaling parameter α for the hot fragments decreases with increasing excitation energy and decreasing symmetry energy. The α values also increase with increasing difference in the isospin (neutron-to-proton asymmetry) of the fragmenting system. A similar behavior is also observed for the cold secondary fragments. The secondary deexcitation is found to have very little influence on the isoscaling parameter at lower excitation energies and isospin of the fragmenting system. The symmetry energy, however, strongly influences the properties of the hot fragments. The experimentally determined isoscaling parameters can be explained by symmetry energy that is significantly lower than that for the normal (cold) nuclei at saturation density, indicating that the properties of nuclei at high excitation energy, isospin, and reduced density are sensitive to the symmetry energy.

The article is organized as follows. In sec. II, we describe the experiment in detail. The experimental results are presented and discussed in Sec. III. Section IV contains a brief description of the statistical multifragmentation model used in the analysis. Section V contains a comparison between the experimental data and the statistical multifragmentation model. Finally, a summary and conclusion is given in Sec. VI.

II. EXPERIMENT

A. Experimental setup

The experiments were carried out at the Cyclotron Institute of Texas A&M University (TAMU) using the K500 Superconducting Cyclotron and the National Superconducting Cyclotron Laboratory (NSCL) at Michigan State University (MSU). Targets of ^{58}Fe (2.3 mg/cm^2) and ^{58}Ni (1.75 mg/cm^2) were bombarded with beams of ^{40}Ar and ^{40}Ca at 33 and 45 MeV/nucleon for the TAMU measurements [42], and targets of ^{58}Fe ($\sim$5 mg/cm^2) and ^{58}Ni ($\sim$5 mg/cm^2) were bombarded with beams of ^{40}Ar and ^{40}Ca at 25 and 53 MeV/nucleon for the NSCL measurements [45]. The various combinations of target and projectile nuclei allowed for a range of N/Z (neutron-to-proton ratio) (1.04–1.23) of the system to be studied, while keeping the total mass constant ($A = 98$).

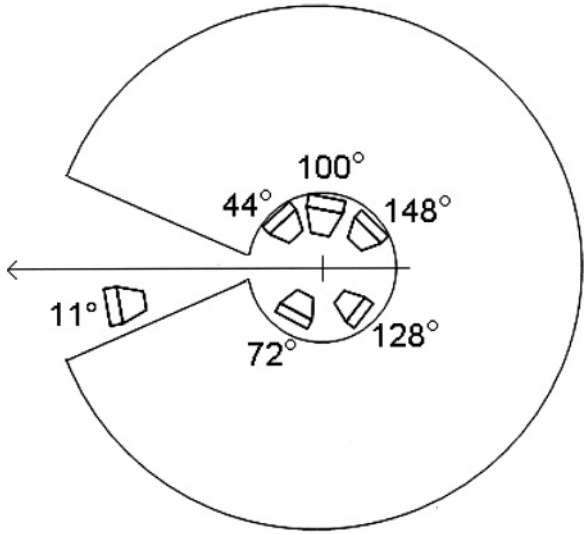

FIG. 1. Schematic diagram of the experimental setup showing the placement of the telescopes inside the scattering chamber of the neutron ball.

The beams in the TAMU measurements were fully stripped by allowing them to pass through a thin aluminum foil before being hit at the center of the target inside the TAMU 4π neutron ball [48]. Light charged particles ($Z \leqslant 2$) and intermediate mass fragments ($Z > 2$) were detected using six discrete telescopes placed inside the scattering chamber of the neutron ball at angles of 10°, 44°, 72°, 100°, 128°, and 148°. A schematic diagram of the setup showing placement of the telescopes within the scattering chamber of the neutron ball is shown in Fig. 1. Each telescope consisted of a gas ionization chamber (IC) followed by a pair of silicon detectors (Si-Si) and a CsI scintillator detector, providing three distinct detector pairs (IC-Si, Si-Si, and Si-CsI) for fragment identification. The ionization chamber was of axial field design and was operated with CF_4 gas at a pressure of 50 torr. The gaseous medium was 6 cm thick with a typical threshold of $\sim$0.5 MeV/nucleon for intermediate mass fragments. The silicon detectors had an active area of 5 × 5 cm and were each subdivided into four quadrants. The first and second silicon detectors in the stack were 0.14 and 1 mm thick, respectively. The dynamical energy range of the silicon pair was $\sim$16–50 MeV for ^{4}He and $\sim$90–270 MeV for ^{12}C. The CsI scintillator crystals that followed the silicon detector pair were 2.54 cm in thickness and were read out by photodiodes. Good elemental (Z) identification was achieved for fragments that punched through the IC detector and stopped in the first silicon detector. Fragments measured in the Si-Si detector pair also had good isotopic separation. Fragments that stopped in CsI detectors showed isotopic resoultion upto $Z = 7$. The trigger for the data acquisition was generated by requiring a valid hit in one of the silicon detectors.

The calibration of the IC-Si detectors were carried out using the standard α sources and by operating the IC at various gas pressures. The Si-Si detectors were calibrated by measuring the energy deposited by the α particles in the thin silicon and the punch-through energies of different isotopes

in the thick silicon. The Si-CsI detectors were calibrated by selecting points along the different light charged isotopes and determining the energy deposited in the CsI crystal from the energy loss in the calibrated Si detector.

The setup for the NSCL experiment consisted of 13 silicon detector telescopes placed inside the MSU 4π Array. Four were placed at 14°, each of which consisted of a 100-μm-thick and a 1-mm-thick silicon surface-barrier detector followed by a 20-cm-thick plastic scintillator. Five telescopes were placed at 40°, in front of the most forward detectors in the main ball of the 4π Array. They each consisted of a 100-μm surface-barrier detector followed by a 5-mm lithium drifted silicon detector. More details are found in Ref. [45]. Good isotopic resolution was obtained as in TAMU measurements.

B. Event characterization

The event characterization of the NSCL data was accomplished by detection of nearly all the coincident charged particles by the MSU 4π Array. Data were acquired using two different triggers, the bulk of which were obtained with the requirement of a valid event in one of the silicon telescopes. Additional data were taken with a minimum bias 4π Array trigger for normalization of the event characterization. The impact parameter of the event was determined by the midrapidity charge detected in the 4π Array as discussed in Ref. [46]. The effectiveness of the centrality cuts was tested by comparing the multiplicity of events from a minimum bias trigger with the multiplicity distribution when a valid fragment was detected at 40° [47]. The minimum bias trigger had a peak multiplicity of charged particles of one, whereas with the requirement of a fragment at 40°, the peak of the multiplicity distribution increased to 5.

The event characterization for the TAMU data was accomplished by using the 4π neutron ball that surrounded the detector assembly. The neutron ball consisted of 11 scintillator tanks segmented in its median plane and surrounding the vacuum chamber. The upper and the lower tank were 1.5-m-diameter hemispheres. Nine wedge-shaped detectors were sandwiched between the hemispheres. All the wedges subtended 40° in the horizontal plane. The neutron ball was filled with a pseudocumene-based liquid scintillator mixed with 0.3 weight percentage of Gd salt (Gd 2-ethyl hexanoate). Scintillations from thermal neutrons captured by Gd were detected by twenty 5-in. phototubes (five in each hemisphere, one on each of the identical 40° wedges and two on the forward edges). The efficiency with which the neutrons could be detected is about 83%, as measured with a ^{252}Cf source.

The detected neutrons were used to differentiate between the central and peripheral collisions. To understand the effectiveness of neutron multiplicity as a centrality trigger, simulations were carried out using hybrid BUU-GEMINI calculations at various impact parameters for the ^{40}Ca+^{58}Fe reaction at 33 MeV/nucleon. The simulated neutron multiplicity distribution was compared with the experimentally measured distribution. The multiplicity of neutron for the impact parameter $b = 0$ collisions was found to be higher than the $b = 5$ collision. By gating on the 10% highest neutron multiplicity events, one could clearly discriminate against the peripheral events.

To determine the contributions from noncentral impact parameter collisions, neutrons emitted in coincidence with fragments at 44° and 152° were calculated at $b = 0$ fm and $b = 5$ fm. The number of events were adjusted for geometrical cross sectional differences. A ratio was made between the number of events with a neutron multiplicity of at least six, calculated at $b = 0$ fm, and the number of events with the same neutron multiplicity at $b = 5$ fm. The ratios were observed to be 19.0 and 11.1 at 44° and 1.3 and 2.2 at 152° for 33 and 45 MeV/nucleon respectively. At intermediate angles, high neutron multiplicities were observed to be outside the region in which $b = 5$ fm contributes significantly. At backward angles the collisions at $b = 5$ fm made a larger contribution to the neutron multiplicity.

In addition to the neutron multiplicity distribution, the charge distribution of the fragments was also used to investigate the contributions from central and mid-impact parameter collisions. The $b = 5$ collisions produced essentially no fragments with charge greater than three in the 44° telescope.

In an earlier work [42], some analysis of the fragment kinetic energy and charge distributions were presented. It was shown that at a laboratory angle of 44° the kinetic energy and the charge distributions are well reproduced by the statistical model calculation. Using a moving source analysis of the fragment energy spectra, it was also shown that the fragments emitted at backward angles originate from a target-like source, whereas those emitted at 44° originate primarily from a composite source. In this work, we will concentrate exclusively on data from the laboratory angle of 44°, which corresponds to the center of mass angle $\approx 90^\circ$, to study the symmetry energy and the isoscaling properties of the fragments produced. The choice of this angle enables one to select events which are predominantly central and undergo bulk multifragmentation. The contributions to the intermediate mass fragments from the projectile-like and targetlike sources can therefore be assumed to be minimal.

III. EXPERIMENTAL RESULTS

A. Relative fragment yield

The experimentally measured relative isotopic yield distributions for the lithium (left), berillium (center), and carbon (right) elements, in ^{40}Ca+^{58}Ni (star symbols), ^{40}Ar+^{58}Ni (circle symbols), and ^{40}Ar+^{58}Fe (square symbols) reactions, are shown in Fig. 2 for the beam energies of 25, 33, and 45 MeV/nucleon. The distributions for each element show higher fragment yield for the neutron-rich isotopes in ^{40}Ar+^{58}Fe reaction (squares), which has the largest neutron-to-proton ratio (N/Z), in comparison to the ^{40}Ca+^{58}Ni reaction (stars), which has the smallest neutron-to-proton ratio. The yields for the reaction ^{40}Ar+^{58}Fe (circles), which has an intermediate value of the neutron-to-proton ratio, are in between those of the other two reactions. The figure thus shows the isospin dependence of the composite system on the properties of the fragments produced in the multifragmentation reaction. One also observes that the relative difference in

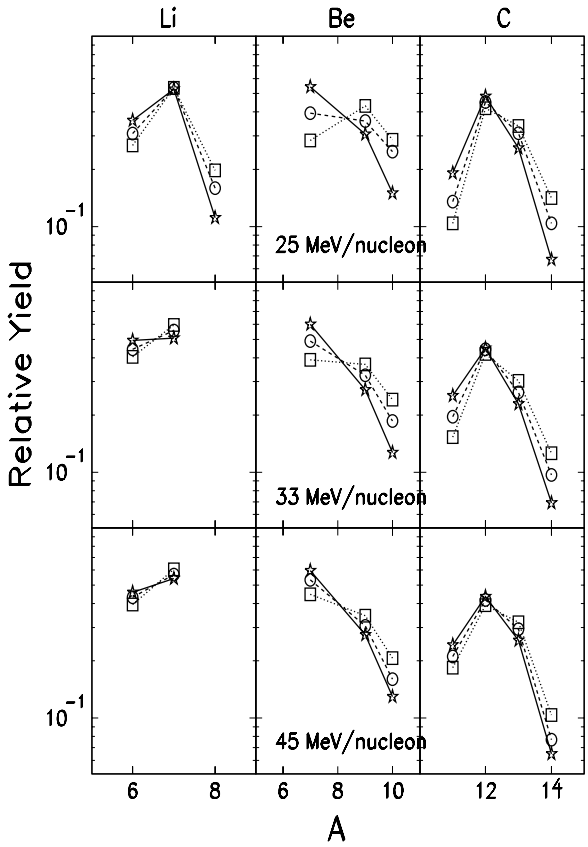

FIG. 2. Relative isotopic yield distribution for the lithium (left), berillium (center) and carbon elements in ^{40}Ca+^{58}Ni (stars and solid lines), ^{40}Ar+^{58}Ni (circles and dashed lines), and ^{40}Ar+^{58}Fe (squares and dotted lines) reactions at various beam energies.

the yield distribution between the three reactions decreases with increasing beam energy. This is due to the secondary deexcitation of the primary fragments, a process that becomes important for systems with increasing neutron-to-proton ratio and excitation energy. In the following subsections, we utilize the experimentally determined isotopic yield distributions to establish the isoscaling properties of the produced fragments before comparing them with the statistical multifragmentation model in Sec. V.

B. Isotopic and isotonic scaling

In a multifragmentation reactions, the ratio of isotope yields in two different systems, 1 and 2, $R_{21}(N, Z) = Y_2(N, Z)/Y_1(N, Z)$, has been shown to obey an exponential dependence on the neutron number (N) and the proton number (Z) of the isotopes, an observation known as isoscaling [5,25,26,49]. The dependence is characterized by a simple relation,

$$R_{21}(N, Z) = Y_2(N, Z)/Y_1(N, Z) = C\exp(\alpha N + \beta Z), \quad (1)$$

where Y_2 and Y_1 are the yields from the neutron-rich and neutron-deficient systems, respectively. C, is an overall normalization factor and α and β are the parameters characterizing the isoscaling behavior.

TABLE I. Double isotope ratios used for the present study and their difference in binding energies.

Double isotope ratio	ΔB (MeV)
(^{7}Li/^{8}Li)/(^{3}He/^{4}He)	−18.54
(^{9}Be/^{10}Be)/(^{3}He/^{4}He)	−13.77
(^{6}Li/^{7}Li)/(^{3}He/^{4}He)	−13.33
(^{10}B/^{11}B)/(^{3}He/^{4}He)	−9.12
(^{7}Li/^{8}Li)/(^{6}Li/^{7}Li)	−5.22
(^{9}Be/^{10}Be)/(^{6}Li/^{7}Li)	−0.44
(^{10}B/^{11}B)/(^{6}Li/^{7}Li)	4.21
(^{9}Be/^{10}Be)/(^{7}Li/^{8}Li)	4.78
(^{10}B/^{11}B)/(^{7}Li/^{8}Li)	9.42

The necessary condition for observing isoscaling in multifragmentation reaction is the near equality of temperature for systems chosen in the above scaling relation [50]. For the present work, this condition was tested by determining the temperature using the double isotope ratio method of Albergo *et al.* [51]. The Albergo method relates the apparent temperature T of the system at the freeze-out to the double isotope ratio, $R = [Y(N, Z_1)/Y(N + 1, Z_1)]/[Y(N, Z_2)/Y(N + 1, Z_2)]$, through a relation

$$T = \frac{\Delta B}{\ln(aR)}, \quad (2)$$

where a is a factor that depends on the statistical weights of the ground-state nuclear spins and $\Delta B = [B(N, Z_1) - B(N + 1, Z_1)] - [B(N, Z_2) - B(N + 1, Z_2)]$ is the difference in the binding energy. The method was applied to all the three systems and beam energies studied. Table I shows the various isotopes used for the double isotope ratios. It should be noted that the goal of temperature determination in this work was only to verify the near equality of the temperatures/excitation energy achieved in various systems for the isoscaling analysis and not as a mean to determine their absolute values. The corrections due to the sequential decay effect were applied whenever available using the values for a from the work of Tsang *et al.* [52].

Figure 3 shows the double isotope ratios obtained using the various combinations of isotopes as a function of the difference in the binding energy. The top panel corresponds to the ratios determined for the beam energies of 25 MeV/nucleon, the center for the 45 MeV/nucleon, and the bottom for the 53 MeV/nucleon. The different symbols correspond to the three different reactions studied. The isotope ratios for the three reactions at each beam energy overlap nicely indicating formation of composite systems with similar temperature/excitation energy. The slopes of the exponential fits to the data (shown by the solid line), which correspond to the apparent temperatures of the systems, show a gradual decrease with increasing beam energy indicating an increase in the excitation energy/temperature of the system.

Having satisfied the necessary condition for isoscaling, the isotopic yield ratio as a function of neutron number N for the beam energies of 25, 33, 45, and 53 MeV/nucleon is plotted in Fig 4. The left column shows the ratio for the ^{40}Ar+^{58}Fe and

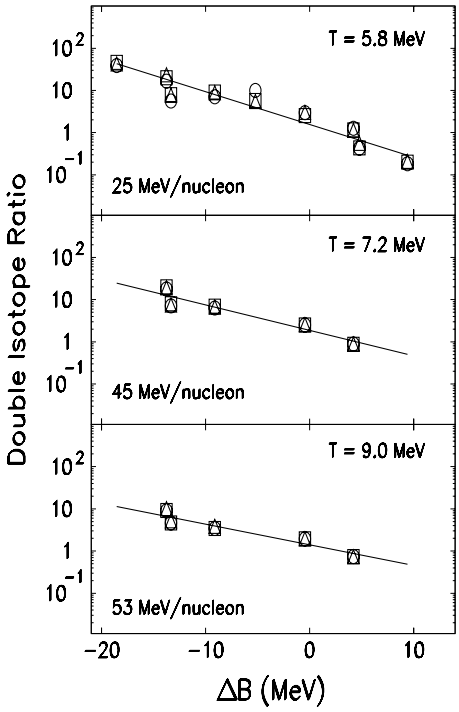

FIG. 3. Double isotope ratio as a function of the difference in binding energy for various beam energies. The circle symbols correspond to ^{40}Ca+^{58}Ni reaction, square symbols to ^{40}Ar+^{58}Ni reaction, and triangle symbols to ^{40}Ar+^{58}Fe reaction. The solid lines are the best fit to the data.

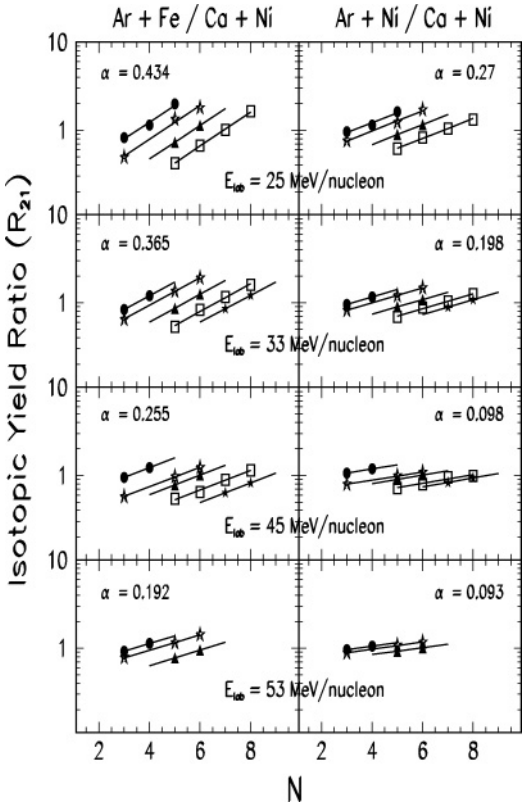

FIG. 4. Experimental isotopic yield ratios of the fragments as a function of neutron number N for various beam energies. The left column correspond to the ^{40}Ar+^{58}Fe and ^{40}Ca+^{58}Ni pair of reactions. The right column correspond to the ^{40}Ar+^{58}Ni and ^{40}Ca+^{58}Ni pair of reactions. The different symbols correspond to $Z = 3$ (circles), $Z = 4$ (open stars), $Z = 5$ (triangles), $Z = 6$ (squares), and $Z = 7$ (filled stars) elements. The lines are the exponential fits to the data as explained in the text.

^{40}Ca+^{58}Ni pair of reaction and the right column shows the ratio for the ^{40}Ar+^{58}Ni and ^{40}Ca+^{58}Ni pair of reaction. One observes that the ratio for each element lies along a straight line in the logarithmic plot and aligns with the neighboring element quite well. This feature is observed for all the beam energies and both pairs of reactions studied. One observes that the alignment of the data points varies with beam energies as well as the pairs of reaction. To have a quantitative estimate of this variation, the ratio for each element (Z) was simultaneously fit using an exponential relation (shown by the solid lines) to obtain the slope parameter α. The values of the parameters are shown at the top of each panel in the figure. The value of the slope parameter α is larger for the ^{40}Ar+^{58}Fe and ^{40}Ca+^{58}Ni reactions, which has a larger difference in the N/Z of the systems in the pair, compared to the ^{40}Ar+^{58}Ni and ^{40}Ca+^{58}Ni reactions, which has a smaller difference in the corresponding N/Z. The α value furthermore decreases with increasing beam energy. Figure 5 shows the isotonic yield ratio as a function of atomic number Z, for the same beam energies and pairs of systems as shown in Fig. 4. Once again, one observes the ratios for each isobar to align nicely with each other at all beam energies. The scaling parameters β in this case, shows an increase with increasing beam energy. The values of the β parameter are larger for the ^{40}Ar+^{58}Ni/^{40}Ca+^{58}Ni reaction pair compared to the ^{40}Ar+^{58}Fe/^{40}Ca+^{58}Ni reaction pair. Figure 6 shows a relative comparison of how the α and β parameters evolve as a function of beam energy and the isospin of the system.

The temperature/excitation energy dependence of the isoscaling properties can be further studied by constructing the scaling factor, $S(\beta, N) = R_{21}(N, Z)e^{-\beta Z}$. The scaling factor is known to be a robust feature over a large range of data, from deep inelastic heavy-ion reactions at lowest energies through evaporation reactions induced by light-ion and heavy-ion projectiles to high-energy heavy-ion reactions characterized by intermediate mass fragments and multifragmentation [26]. With a single value for the β parameter, all the isotopes should fall along a single line in a plot of $S(\beta, N)$ vs N. This is shown in Fig. 7, where the $S(\beta, N)$ from two different reaction pairs are plotted as a function of neutron number N for beam energies of 25 and 45 MeV/nucleon. The parameter β, was taken from the fit to the isotonic yield ratio shown in Fig. 5. As shown in Fig. 7, the values of $S(\beta, N)$ obtained from various elements (Z) cluster and scale along a single line. The figure shows a significant difference in the scaling for the two beam energies, indicating the influence of temperature on the isotopic yields of the light clusters. The present observation alternatively demonstrates the role played by the temperature in the distillation of nuclear matter into a neutron-rich gas and a

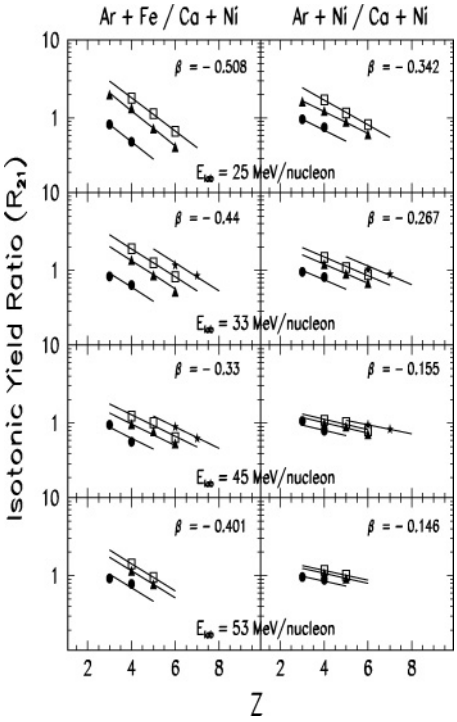

FIG. 5. Experimental isotonic yield ratios of the fragments as a function of proton number Z for various beam energies. The left column correspond to the ^{40}Ar+^{58}Fe/^{40}Ca+^{58}Ni pair of reaction. The right column correspond to ^{40}Ar+^{58}Ni/^{40}Ca+^{58}Ni pair of reaction. The different symbols correspond to $N = 3$ (circles), $N = 5$ (triangles), $N = 6$ (squares), and $N = 7$ (stars) elements. The lines are the exponential fits to the data as explained in the text.

more symmetric liquid phase. We illustrate this further in the following section.

C. Isospin fractionation and the reduced nucleon densities

In grand canonical approach of the multifragmentation process (see, e.g., Refs. [51,53–55]), the fragment yield with neutron number N and proton number Z (mass number $A = N + Z$) can be written as

$$Y(N, Z) \propto V \rho_n^N \rho_p^Z Z_{N,Z}(T) A^{3/2} e^{B(N,Z)/T}, \qquad (3)$$

where V is the volume of the system and $\rho_n (\propto e^{\mu_n/T})$ and $\rho_p (\propto e^{\mu_p/T})$ are the primary "free" neutron and proton densities. The exponents μ_n and μ_p are the neutron and the proton chemical potentials, and $Z_{N,Z}(T)$ is the intrinsic partition function of the excited fragment. The quantity $B(N, Z)$, is the ground-state binding energy of the fragment and T is the temperature. In the above formula, the effect of Coulomb interaction on fragment yield is neglected by introducing ρ_n and ρ_p. The actual isotope yields then reduce to an approximation appropriate for the thermodynamical limit at high excitation energy [53]. As discussed in the introduction, taking the ratios of the fragment yields from two different systems that differ only in their isospin (N/Z) content reduces the uncertainties in the quantities shown in Eq. (3). The isotopic yield distribution of the fragments in terms of relative reduced neutron density can

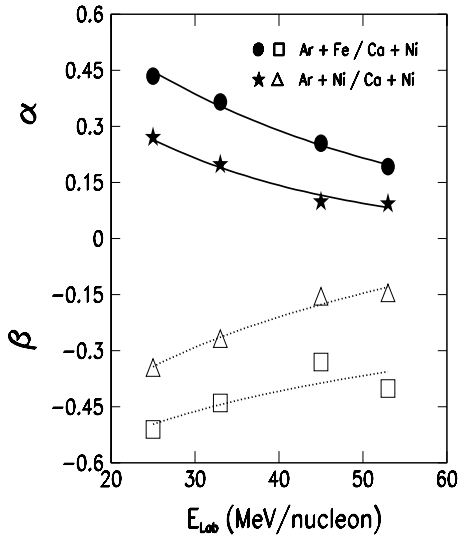

FIG. 6. Isoscaling parameters α (solid symbols) and β (open symbols) as a function of the beam energy. The solid circles and open squares correspond to ^{40}Ar+^{58}Fe/^{40}Ca+^{58}Ni pair of reactions. The solid stars and open triangles correspond to ^{40}Ar+^{58}Ni/^{40}Ca+^{58}Ni pair of reactions. The lines are the exponential fits to the data. The error bars are of the size of the symbols.

then be written as

$$\frac{Y(N+k, Z)/Y^{\mathrm{Ca+Ni}}(N+k, Z)}{Y(N, Z)/Y^{\mathrm{Ca+Ni}}(N, Z)} = \left(\frac{\rho_n}{\rho_n^{\mathrm{Ca+Ni}}}\right)^k, \qquad (4)$$

where k corresponds to various isotopes of an element that can be used to determine the double ratio. The quantity $Y^{\mathrm{Ca+Ni}}$ is the yield for the ^{40}Ca+^{58}Ni reaction with respect to which all the ratios are taken in this work. A similar expression for the relative reduced proton density from the isotonic yield ratios can also be written as

$$\frac{Y(N, Z+k)/Y^{\mathrm{Ni+Ni}}(N, Z+k)}{Y(N, Z)/Y^{\mathrm{Ca+Ni}}(N, Z)} = \left(\frac{\rho_p}{\rho_p^{\mathrm{Ca+Ni}}}\right)^k. \qquad (5)$$

In the statistical limit for a dilute noninteracting gas, the relative nucleon densities are related to the isoscaling parameters α and β through a relation $\rho_n^{\mathrm{Ar+Fe}}/\rho_n^{\mathrm{Ca+Ni}} = e^{\alpha}$ and $\rho_p^{\mathrm{Ar+Fe}}/\rho_p^{\mathrm{Ca+Ni}} = e^{\beta}$, where $\alpha = \Delta\mu_n/T$ and $\beta = \Delta\mu_p/T$, with $\Delta\mu_n$ and $\Delta\mu_p$ being the difference in neutron and proton chemical potentials.

In Fig. 8, we show the experimentally obtained relative reduced neutron and proton density as a function of the difference in the N/Z of the systems for the Ar + Ni/Ca + Ni and Ar + Fe/Ca + Ni pairs of reactions. All densities shown are relative to those of Ca + Ni reaction. The circle symbols correspond to the 25 MeV/nucleon, squares to the 33 MeV/nucleon, and the triangles to the 45 MeV/nucleon beam energies. The α and the β values were taken from the fit to the isotopic and isotonic yield ratios of Figs. 4 and 5. The figure shows a steady decrease in the reduced neutron density and an increase in the proton density with increasing beam energies. The effect is stronger for the ^{40}Ar+^{58}Fe and ^{40}Ca+^{58}Ni reaction pair that has the highest difference in N/Z.

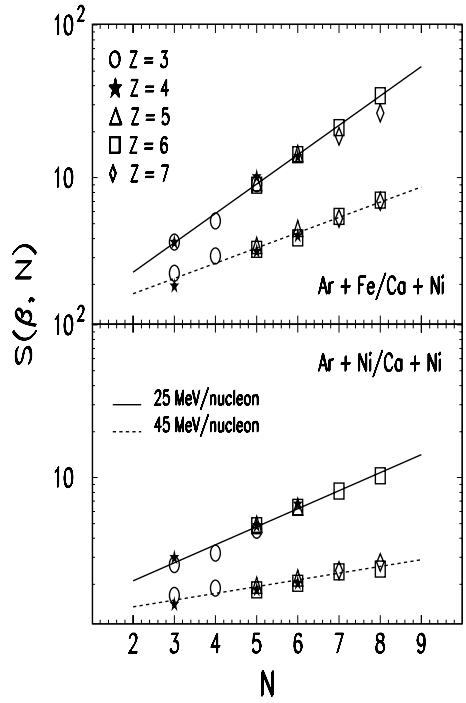

FIG. 7. The scaled isotope ratio $S(\beta, N)$, as a function of the neutron number N for the 25 and 45 MeV/nucleon beam energies. The top panel is for the ^{40}Ar+^{58}Fe/^{40}Ca+^{58}Ni pair, and the bottom panel is for the ^{40}Ar+^{58}Ni/^{40}Ca+^{58}Ni pair of reactions. The symbols correspond to $S(\beta, N)$ obtained from various elements (Z). The lines are the best fits to the data.

An important feature of the data shown in Fig. 8 is the decrease in the relative neutron-proton asymmetry $(\rho_n/\rho_n^{\mathrm{Ca+Ni}} - \rho_p/\rho_p^{\mathrm{Ca+Ni}})$ with increasing beam energy. The asymmetry is found to decrease from ∼1.0 at 25 MeV/nucleon to ∼0.6 at 45 MeV/nucleon for the Ar + Fe/Ca + Ni pair of reaction. The observed decrease indicates a decrease in the sensitivity of the isospin effect with increasing temperature.

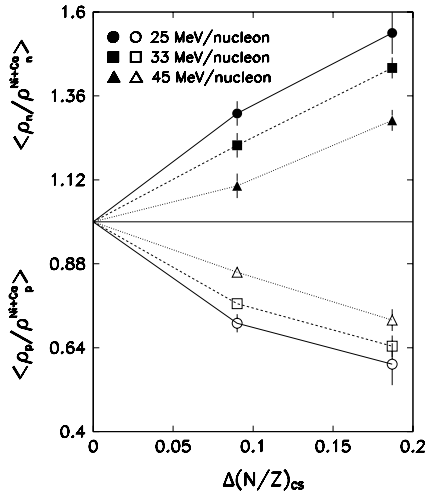

FIG. 8. Relative free neutron (solid symbols) and proton (open symbols) densities as a function of the difference in N/Z of the systems for the beam energies of 25, 33, and 45 MeV/nucleon.

As mentioned earlier in this section, the relative neutron density is related to the isoscaling parameter α. In the following sections, we investigate the relationship between the isoscaling parameter and the symmetry energy of the fragment using the statistical multifragmentation model.

IV. STATISTICAL MULTIFRAGMENTATION MODEL

Statistical models [53–58] are widely used for describing multifragmentation reactions [37,59–64]. They are based on the assumption of statistical equilibrium at a low-density freeze-out stage. In the statistical multifragmentation model (SMM) [53,66], all breakup channels composed of nucleons and excited fragments are taken into account and considered as partitions. During each partition, the conservation of mass, charge, energy, and angular momentum is taken into account, and the partitions are sampled uniformly in the phase space according to their statistical weights using the Monte Carlo sampling. In the present calculations the Coulomb interaction between the fragments is treated in the Wigner-Seitz approximation. Light fragments with mass number $A \leqslant 4$ are considered as elementary particles with only translational degrees of freedom ("nuclear gas"). Fragments with $A > 4$ are treated as heated nuclear liquid drops, and their individual free energies $F_{A,Z}$ are parametrized as a sum of the volume, surface, Coulomb, and symmetry energy,

$$F_{A,Z} = F^V_{A,Z} + F^S_{A,Z} + E^C_{A,Z} + E^{\mathrm{sym}}_{A,Z}, \tag{6}$$

where $F^V_{A,Z} = (-W_o - T^2/\epsilon_o)A$, with parameter ϵ_o related to the level density and $W_o = 16$ MeV being the binding energy of infinite nuclear matter. $F^S_{A,Z} = B_o A^{2/3}[(T_c^2 - T^2)/(T_c^2 + T^2)]^{5/4}$, with $B_o = 18$ MeV being the surface coefficient and $T_c = 18$ MeV being the critical temperature of infinite nuclear matter. $E^C_{A,Z} = cZ^2/A^{1/3}$, where $c = (3/5)(e^2/r_o)[1 - (\rho/\rho_o)^{1/3}]$, is the Coulomb parameter obtained in the Wigner-Seitz approximation with charge unit e, and $r_o = 1.17$ fm. $E^{\mathrm{sym}}_{A,Z} = \gamma(A - 2Z)^2/A$, where $\gamma = 25$ MeV is the symmetry energy coefficient. These parameters are those adopted from the Bethe-Weizsacker mass formula and correspond to the assumption of isolated fragments with normal density in the freeze-out configuration. The value of the symmetry energy coefficient γ is taken from the fit to the binding energies of isolated cold nuclei in their ground states. In a multifragmentation process the primary fragments are not only excited but also expanded. The fragments continue to interact in-medium with each other inside the freeze-out volume and modify their parameters. By comparing the experimentally determined fragment yield distribution with the SMM calculation, the parameters of hot nuclei under multifragmentation conditions, including the symmetry energy, can be extracted. In the following, it will be shown how this information can be obtained from the isoscaling phenomena.

A. Isoscaling and symmetry energy coefficient

Isotopic scaling or isoscaling arise naturally in statistical equilibrium models of multifragmentation. In these models the

difference in the chemical potential of systems with different N/Z is directly related to the scaling parameter α. It has been shown that the isoscaling parameter α is proportional to the symmetry energy part of the fragment binding energy through a relation,

$$\alpha = \frac{4\gamma}{T}\left(\frac{Z_1^2}{A_1^2} - \frac{Z_2^2}{A_2^2}\right) \tag{7}$$

where Z_1, A_1 and Z_2, A_2 are the charge and the mass numbers of the fragmenting systems, T is the temperature of the system and γ, the symmetry energy coefficient [5].

B. Secondary deexcitation of the fragments

The above formula in the statistical model approach is valid at the freeze-out stage where the primary hot fragments are formed at reduced density. To extract information on symmetry energy γ from the observed cold secondary fragments, one has to take into account the process of secondary deexcitation. In SMM, the secondary deexcitation of large fragments with $A > 16$ is described by Weisskopf-type evaporation and Bohr-Wheeler-type fission models [53,55]. The decay of smaller fragments is treated with the Fermi-breakup model. All ground and nucleon-stable excited states of light fragments are taken into account and the population probabilities of these states are calculated according to the available phase space [55].

V. COMPARISON WITH THE EXPERIMENTAL DATA

To compare the experimentally observed results to the theoretical predictions, we have calculated the primary and the secondary fragment isotopic yield distributions using the above-described SMM. The calculations were carried out for the ^{40}Ca+^{58}Ni,^{40} Ar+^{58}Ni, and ^{40}Ar+^{58}Fe reactions at various excitation energies. The excitation energy per nucleon of the initial system for the calculation depends strongly on the matching condition between the dynamical and statistical stage of the collision. This quantity is presently difficult to calculate accurately. A range of values for the excitation energy per nucleon from $E^* = 4$–10 MeV/nucleon was therefore assumed. The excitation energy corresponding to each beam energy was also verified by an independent calculation using BUU-GEMINI (see Table II in Ref. [42]) and the systematic calorimetric measurements available in the literature for systems with mass $A \sim 100$ [65]. The mass and the charge of the initial systems were assumed to be those of the initial compound nucleus. It must be mentioned that the preequilbrium emission during the initial stages of the compound nucleus evolution, as observed in the dynamical calculations of Li *et al.* [43], could affect the initial charge and mass of the source depending on the stiffness of the nuclear equation of state. In the present analysis, the Z/A of the source was estimated from the dynamical BNV calculation [44]. These results were obtained [1] at a time around 50 fm/c after the projectile fuses with the target nuclei and the quadrupole moment of the nucleon coordinates approaches zero. The observed change was about 3% lower than the initial Z/A of the system. However, this change depends on the time at which the dynamical code is terminated, and we have therefore chosen not to include any change in Z/A in this analysis. To account for the possible uncertainty in the source size due to the loss of nucleons during preequilibrium emission, the SMM calculation was also carried out for sources with 80% of the total mass. No significant change in the isospin characteristics under study was observed. The freeze-out density in the calculation was assumed to be 1/3 of the normal nuclear density and the symmetry energy coefficient γ was taken to be 25 MeV.

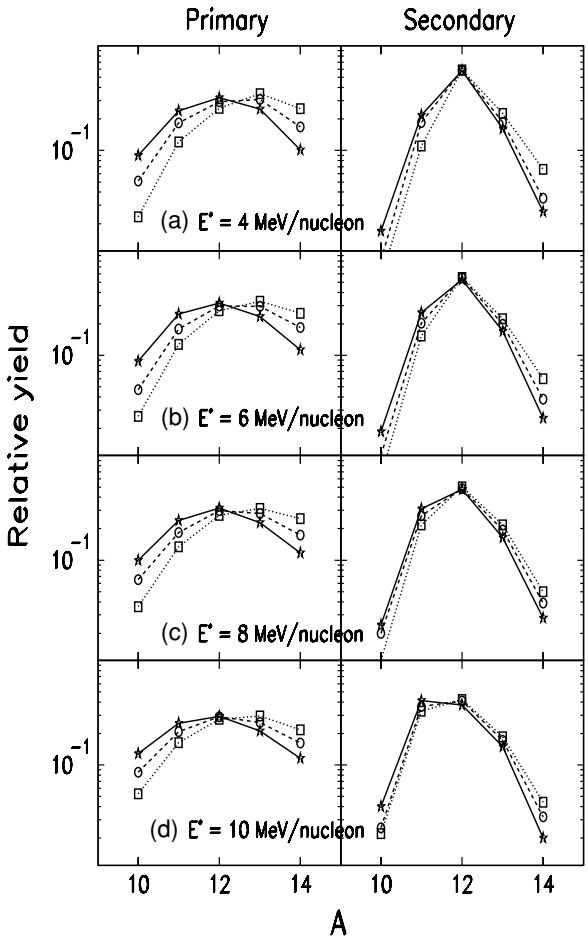

FIG. 9. SMM calculated primary (left) and secondary (right) fragment isotope yield distributions for the carbon element in ^{40}Ca+^{58}Ni (stars and solid lines), ^{40}Ar+^{58}Ni (circles and dashed lines), and ^{40}Ar+^{58}Fe (squares and dotted lines) reactions at various excitation energies. The calculations are for $\gamma = 25$ MeV.

The calculated primary and secondary fragment yield distributions for the Carbon isotopes in ^{40}Ca+^{58}Ni,^{40} Ar+^{58}Ni, and ^{40}Ar+^{58}Fe reactions at various excitation energies are as shown in Fig. 9. The characteristics of the hot primary fragment yield distribution, shown in the left column of the figure, change significantly after the secondary deexcitation. The primary yield distribution for the three systems, shown by the dotted, dashed, and solid curve, for each excitation energy clearly shows an isospin effect. The most neutron rich system has the largest yield for the neutron-rich isotopes and the lowest yield for the neutron-deficient isotopes. This effect appears to decrease with increasing excitation energy. A similar feature

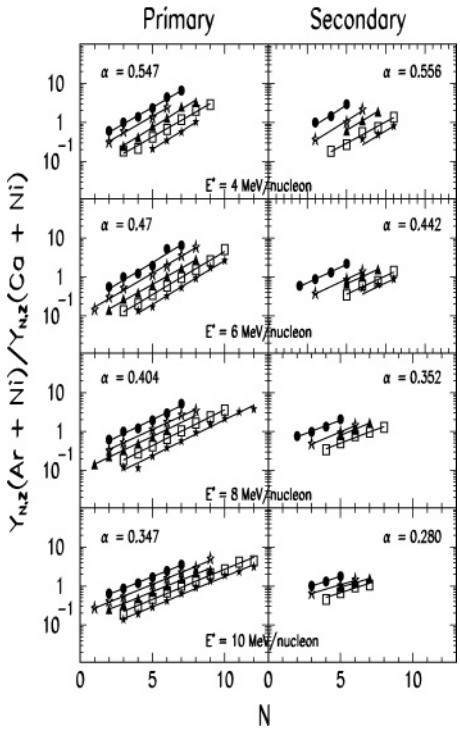

FIG. 10. Calculated isotopic yield ratios from the primary (left) and the secondary (right) fragment yield distributions for the ^{40}Ar+^{58}Ni and ^{40}Ca+^{58}Ni pairs at various excitation energies. The calculations are for $\gamma = 25$ MeV. The different symbols shown correspond to $Z = 3$ (circles), $Z = 4$ (open stars), $Z = 5$ (triangles), $Z = 6$ (square), and $Z = 7$ (solid stars) elements. The lines are the exponential fits to the ratios.

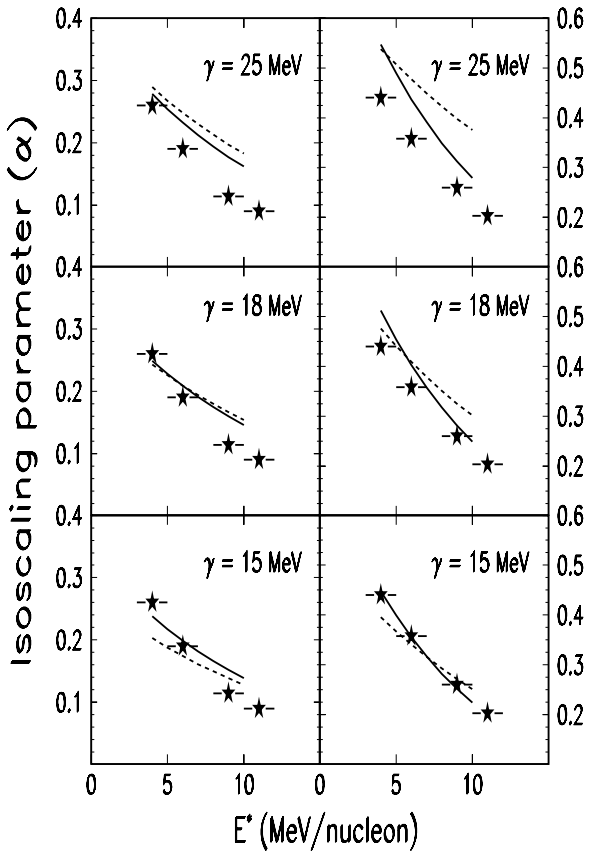

FIG. 11. Comparison of the SMM calculated α (lines) with the experimentally determined α (symbols) as a function of excitation energy for different values of the symmetry energy coefficient γ. The dotted lines correspond to the primary fragments and the solid lines to the secondary fragments. The left column shows the comparison for the ^{40}Ar+^{58}Ni and ^{40}Ca+^{58}Ni pair, and the right column shows the comparison for the ^{40}Ar+^{58}Fe and ^{40}Ca+^{58}Ni pair.

is also observed in the secondary fragment distribution shown in the right column of the figure, though the effect is observed to be weakened significantly. Furthermore, the mean of the distribution is also observed to decrease along with the width for the secondary fragments. Qualitatively, the SMM simulates quite well the overall features of the experimentally observed isotopic yield distribution shown in Fig. 2. The isotopic yield ratios using the primary and the secondary fragment distribution from the statistical multifragmentation model are shown in Fig. 10 for the ^{40}Ar+^{58}Ni and ^{40}Ca+^{58}Ni pair of reaction. It is observed that the yield ratios for both the primary and the secondary distribution obey the isoscaling relation quite well. Very little difference is observed in the scaling parameter α, obtained from the primary and the secondary yield distribution. Furthermore, the scaling parameter shows a gradual decrease in its value with increasing excitation energy similar to those observed experimentally and shown in Fig. 6.

Though the overall feature of the scaling parameter calculated from the statistical multifragmentation model is reproduced quite well, the absolute values do not quite agree with the experimentally determined α. This is shown in the top panel of Fig. 11, where a comparison is made between the SMM calculated and the experimentally observed values of α. In the figure, the left column corresponds to the ^{40}Ar+^{58}Ni and ^{40}Ca+^{58}Ni pair of reactions and the right to the ^{40}Ar+^{58}Fe and ^{40}Ca+^{58}Ni pair. The dotted lines correspond to the α calculated from the primary fragment distributions and the solid lines to those calculated from the secondary fragment distributions. The symbols correspond to the experimentally determined αs. It is observed that the experimentally determined αs are significantly lower than the calculated values of α using the standard value of the symmetry energy coefficient, $\gamma =$ 25 MeV, for the isolated cold nuclei in their ground states. To explain the observed dependence of the isoscaling parameter α on excitation energy, we varied the γ of the hot primary fragment in the SMM input in the range 25–15 MeV. As shown in the center and the bottom panel of the figure, the isoscaling parameter decreases slowly with decreasing symmetry energy. The experimentally determined α could be reproduced for both pairs of systems at all excitation energies using a symmetry energy value of $\gamma = 15$ MeV. This value of symmetry energy is significantly lower than the value of $\gamma = 25$ MeV used for ground-state nuclei. The decrease in the symmetry energy results in an increase in the width of the isotopic yield distribution making them more neutron-rich. In Fig. 12, we show a comparison between the experimentally determined carbon isotopic yield distribution and the SMM calculated yield distribution, using two different values of the

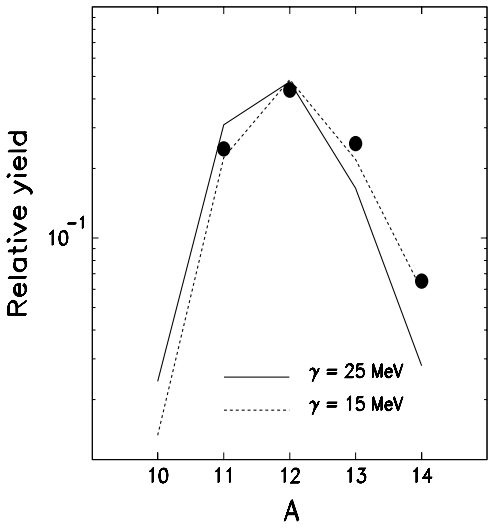

FIG. 12. Isotopic yield distribution for the carbon element in ^{40}Ca+^{58}Ni reaction at 45 MeV/nucleon. The solid line is the SMM calculation with symmetry energy coefficient $\gamma = 25$ MeV, and the dashed line is the calculation with $\gamma = 15$ MeV. The solid points correspond to the experimental result.

fragment symmetry energy. As shown, a lower value of the symmetry energy (γ) is required to explain the experimental yield distribution.

Figure 13 shows the calculated γ dependence of the isoscaling parameter α from the hot primary fragment distribution, and from the cold secondary fragment distribution, for the two pairs of systems at various excitation energies. The α as a function of symmetry energy for each excitation energy and system is observed to decrease with decreasing symmetry energy. The difference between the primary fragment α and the secondary fragment α is negligible for the Ar+Ni and Ca+Ni reaction pair, which has the lowest difference in neutron-to-proton ratio. The difference for the Ar+Fe and Ca+Ni pair, which has the highest difference in neutron-to-proton ratio, however, is slightly larger at higher excitation energies.

A. Secondary deexcitation of the fragments with changing symmetry

In the above described statistical multifragmentation model calculations the masses of the fragments used were those of cold isolated nuclei. The fragments in their primary stage are usually hot and the properties of hot nuclei (i.e., their binding energies and masses) differ from those of cold nuclei. If hot fragments in the freeze-out configuration have smaller γ, their masses at the beginning of the secondary deexcitation will be different, and this effect should be taken into account in the evaporation process. Recently, Buyukcizmeci *et al.* [67] adopted a phenomenological approach to estimate the effect of the symmetry energy evolution during the sequential evaporation. In this approach, they assume liquid drop masses $m_{A,Z} = m_{\rm ld}(\gamma)$ for the evaporation of the light particles (n, p, d, t,^{3} He, α) if the internal excitation energy of the fragment is large ($\xi = \beta E^*/A > 1$). At lower

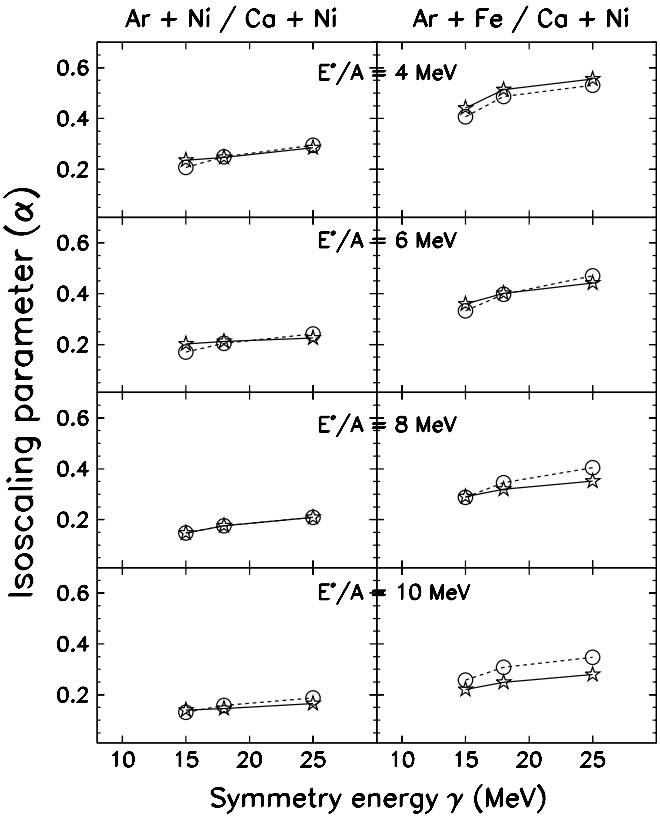

FIG. 13. SMM calculated isoscaling parameter α as a function of symmetry energy coefficient for various excitation energies. The open circles joined by dotted lines correspond to the primary fragments and the open stars joined by solid lines to the secondary fragments. The left column shows the calculation for ^{40}Ar+^{58}Ni and ^{40}Ca+^{58}Ni pair and the right column shows the calculation for the ^{40}Ar+^{58}Fe and ^{40}Ca+^{58}Ni pair.

excitation energies ($\xi \leqslant 1$) they assume a smooth transition to standard experimental masses with shell effects($m_{\rm exp}$) using the following dependence,

$$m_{A,Z} = m_{\rm ld}(\gamma)\xi + m_{\rm exp}(1-\xi). \tag{8}$$

The excitation energy is determined from the energy balance taking into account the mass $m_{A,Z}$ at the given excitation. The above corrections were incorporated in the statistical model calculations described in the previous section to study the effect of γ during the sequential deexcitation of the hot primary fragments. Figure 14 shows the result of the statistical model calculation using the modified secondary deexcitation correction. The isoscaling parameter α is plotted as a function of excitation energy for the two pairs of systems (left and right column). The top panels show the calculations using symmetry energy value of 25 MeV. As noted in the previous section, the new calculations are not able to reproduce the experimentally determined α for both pairs of systems. With decreasing values of the symmetry energy, the calculated α values for the Ar+Ni and Ca+Ni pair (left column) decrease and are in better agreement with the experimental values at $\gamma = 13$ MeV. However, the calculated values for the Ar+Fe and Ca+Ni reaction pair (right column) are in good agreement

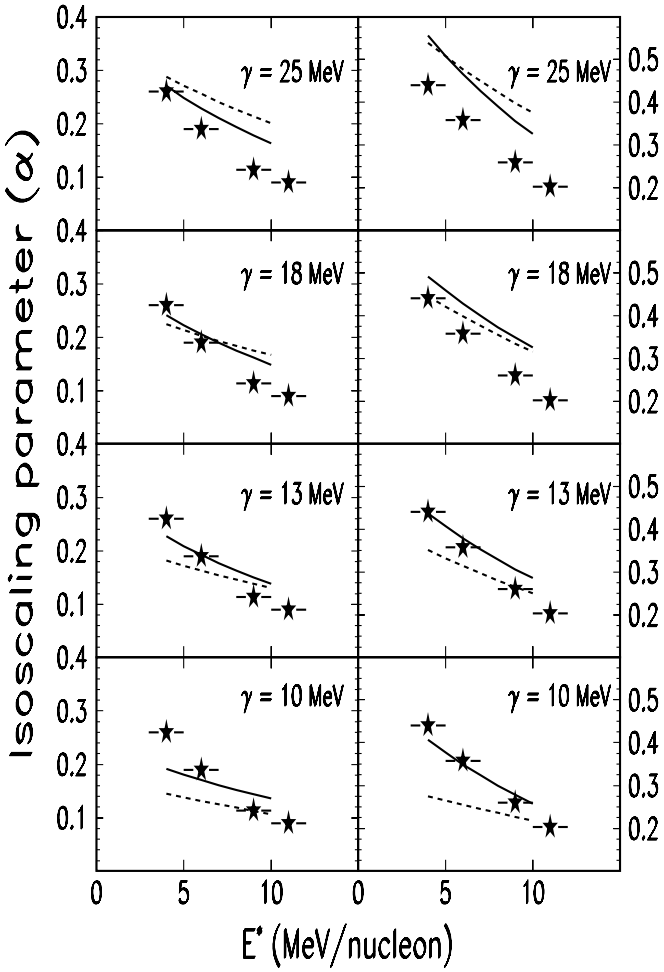

FIG. 14. Same as in Fig. 11, but with the modified secondary deexcitation with evolving symmetry energy coefficient.

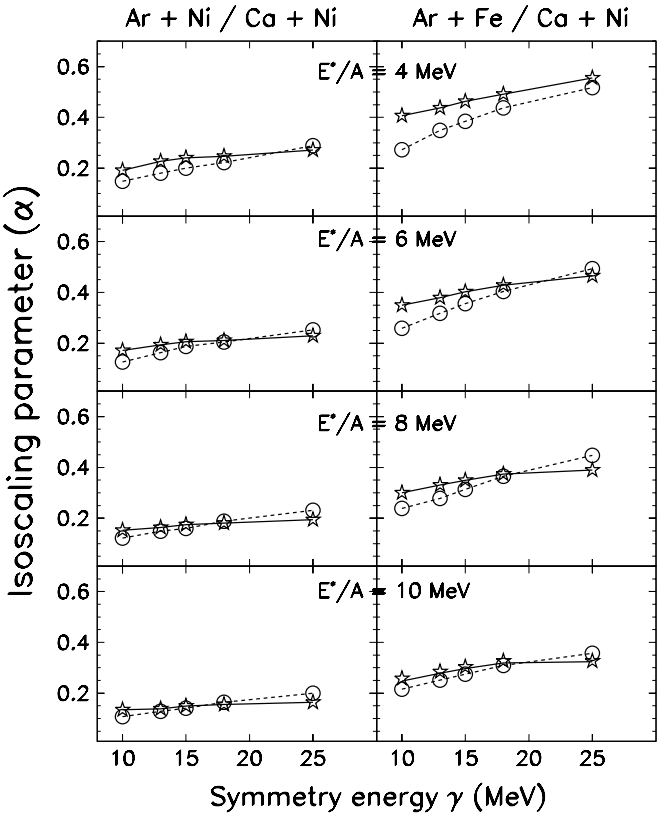

FIG. 15. Same as in Fig. 13, but with the modified secondary deexcitation with evolving symmetry energy coefficient.

with the experimental values at $\gamma = 10$ MeV. In general, one observes that the modified version of secondary deexcitation in SMM leads to a symmetry energy value of 10–13 MeV. This is slightly lower than the value of 15 MeV obtained from the standard version of the SMM calculation shown in Fig. 11.

The dependence of the isoscaling parameter as a function of the symmetry energy for primary and secondary fragments at various excitation energies are as shown in Fig. 15. Once again, the difference between the primary fragment α and the secondary fragment α are extremely small for the Ar+Ni and Ca+Ni pair of reaction (which has the lowest difference in neutron-to-proton ratio), and only slightly larger for the Ar+Fe and Ca+Ni pair (which has the highest difference in neutron-to-proton ratio). However, the main difference between the dependence shown in Figs. 13 and 15 is the rate at which the isoscaling parameter α decrease with decreasing symmetry energy. The decrease is much slower in the calculation where the symmetry energy dependence of the mass is taken into account during the secondary deexcitation. The slower decrease in the isoscaling parameter results in the calculation being able to reproduce the experimental value at a slightly lower value of symmetry energy. One also observes that the primary fragment α in the modified version of the secondary decay calculation are consistently smaller than the secondary fragment α at lower symmetry energies.

To understand the difference in the symmetry energy, we show in Fig. 16, the calculated isotopic yield distribution for the Carbon element in ^{40}Ar+^{58}Fe reaction at $E^* =$ 6 MeV/nucleon. The figure shows the primary and the secondary yield distribution using two different prescriptions for the secondary deexcitations in SMM. The left column in the figure corresponds to the SMM calculations, where the fragment masses used are those of cold isolated nuclei and the right column corresponds to the SMM calculations, where the masses (symmetry energy) evolve with their excitation energy during secondary deexcitation. The panels on the top correspond to the primary yield distribution and those in the bottom to the secondary yield distribution. The dotted and the solid curves in each panel corresponds to the calculations assuming two different values of the symmetry energy, 15 and 25 MeV, respectively. From the figure, it is evident that there exist a subtle difference between the two final (secondary) distributions, shown by the dotted and the solid curves in the bottom panels. One also observes that the distribution depends on whether the mass (symmetry energy) evolves during the evaporation. The SMM calculation with the standard deexcitation (i.e, the old deexcitation) leads to a narrow final distribution and the isotopes are concentrated close to the β-stability line. The difference in the final yield distributions for $\gamma = 15$ MeV and $\gamma = 25$ MeV is very small. This difference is, however, much more pronounced in the

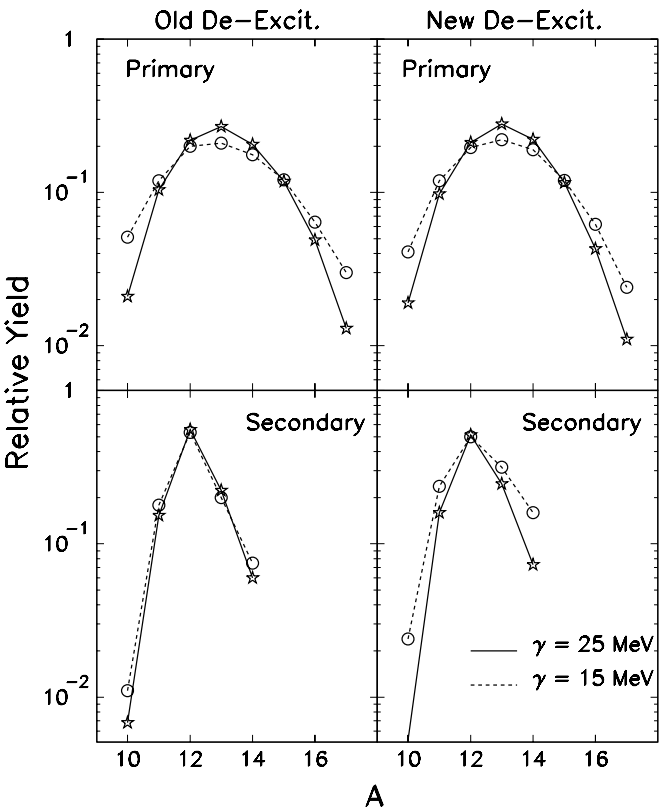

FIG. 16. Comparison between the calculated primary (top) and the secondary (bottom) isotopic yield distribution for the carbon element in ^{40}Ar+^{58}Fe reaction at $E^* = 6$ MeV/nucleon. The left panels correspond to the old and the right to the new deexcitation prescription used in the SMM calculation. The solid and the dashed curves correspond to the calculations using two different values of the symmetry energy.

new deexcitation calculation. The final isotope distributions in this case are considerably wider and shifted toward the neutron-rich side. The SMM calculation assuming the mass (symmetry energy) evolution during the evaporation therefore leads to larger yields for neutron rich fragments. A similar observation was made by Buyukcizmeci *et al.* [67] in their calculation of the primary and secondary fragment isotopic distributions in ^{197}Au,^{124} Sn, and ^{124}La systems. By using the experimental masses during the evaporation from the primary fragments, the emission of the charged particles are suppressed by the binding energy and the Coulomb barrier. In the case of small γ, the binding energy in the beginning of evaporation process essentially favors emission of charged particles. When the nucleus has cooled down sufficiently to restore the normal symmetry energy, the remaining excitation energy is rather low ($E^*/A < 1$ MeV) for the nucleus to evaporate many neutrons.

The above comparison of the experimentally observed isoscaling properties with the statistical multifragmentation model shows that, irrespective of the secondary deexcitation, the final fragment distribution depends strongly on the available free energy and the strength of the symmetry energy. A significantly lower value of the symmetry energy than that assumed for cold isolated nuclei is required to explain the isotopic compositions of the fragments produced in multifragmentation reaction. The difference between the two kinds of evaporation calculations gives a measure of the uncertainty expected in the present analysis. The results above indicate that the properties of nuclei produced at high excitation energy, isospin, and reduced density could be significantly different from those of the cold isolated nuclei. Such information can provide important inputs for the understanding of the nuclear composition of supernova matter where hot and neutron-rich nuclei are routinely produced [4,12].

VI. SUMMARY AND CONCLUSIONS

In summary, we have measured the isotopic yield distribution of the fragments produced in the multifragmentation of ^{40}Ar,^{40} Ca+^{58}Fe,^{58} Ni reactions at 25–53 MeV/nucleon. The symmetry energy and the isoscaling properties of the fragments produced were studied within the framework of statistical multifragmentation model. It is observed that the isoscaling parameter α for the hot fragments decrease with increasing excitation energy and decreasing symmetry energy. The α values increase with increasing difference in the isospin of the fragmenting system. Similar behavior is also observed for the cold secondary fragments. The sequential decay of the primary fragments to secondary fragments is observed to have very little influence on the isoscaling parameter as a function of excitation energies and isospin of the fragmenting system. The symmetry energy, however, strongly influences the isospin properties of the hot fragments. The experimentally determined scaling parameters could be explained by a symmetry energy that is as low as 10–15 MeV and significantly lower than that for the normal (cold) nuclei at saturation density. The present results indicate that the isospin properties of the fragments produced at high excitation energy and reduced density in multifragmentation reaction are sensitive to the symmetry energy.

ACKNOWLEDGMENTS

The authors thank the Cyclotron Institute staff for the excellent beam quality. This work was supported in parts by the Robert A. Welch Foundation through grant A-1266 and the Department of Energy through grant DE-FG03-93ER40773.

[1] D. V. Shetty, A. S. Botvina, S. J. Yennello, G. Souliotis, E. Bell, and A. Keksis, Phys. Rev. C **71**, 024602 (2005).
[2] A. Le Fevre *et al.*, Phys. Rev. Lett. **94**, 162701 (2005).
[3] D. Henzlova, A. S. Botvina, K. H. Schmidt, V. Henzl, P. Napolitani, and M. V. Ricciardi, nucl-ex/0507003 (2005).
[4] A. S. Botvina and I. N. Mishustin, Phys. Lett. **B584**, 233 (2004).
[5] A. S. Botvina, O. V. Lozhkin, and W. Trautmann, Phys. Rev. C **65**, 044610 (2002).
[6] J. M. Lattimer, C. J. Pethick, M. Prakash, and P. Hansel, Phys. Rev. Lett. **66**, 2701 (1991).

[7] C. Lee, Phys. Rep. **275**, 255 (1996).
[8] C. J. Pethick and D. G. Ravenhall, Annu. Rev. Nucl. Part. Sci. **45**, 429 (1995).
[9] J. M. Lattimer and M. Prakash, Phys. Rep. **333**, 121 (2000).
[10] W. R. Hix, O. E. B. Messner, A. Mezzacappa, M. Liebendorfer, J. Sampaio, K. Langanke, D. J. Dean, and G. Martinez-Pinedo, Phys. Rev. Lett. **91**, 201102 (2003).
[11] J. M. Lattimer and M. Prakash, Astrophys. J. **550**, 426 (2001).
[12] A. S. Botvina and I. N. Mishustin, Phys. Rev. C **72**, 048801 (2005).
[13] B. A. Brown, Phys. Rev. Lett. **85**, 5296 (2000).
[14] C. J. Horowitz and J. Piekarewicz, Phys. Rev. Lett. **86**, 5647 (2001).
[15] R. J. Furnstahl, Nucl. Phys. **A706**, 85 (2002).
[16] K. Oyamatsu, I. Tanihata, Y. Sugahara, K. Sumiyoshi, and H. Toki, Nucl. Phys. **A634**, 3 (1998).
[17] A. Ono, P. Danielewicz, W. A. Friedman, W. G. Lynch, and M. B. Tsang, Phys. Rev. C **68**, 051601(R) (2003).
[18] L. W. Chen, C. M. Ko, and B. A. Li, Phys. Rev. Lett. **94**, 032701 (2005).
[19] D. V. Shetty *et al*., Phys. Rev. C **70**, 011601(R) (2004).
[20] M. B. Tsang *et al*., Phys. Rev. Lett. **92**, 062701 (2004).
[21] B. A. Li, C. M. Ko, and W. Bauer, Int. J. Mod. Phys. E **7**, 147 (1998).
[22] V. Baran, M. Colonna, V. Greco, and M. DiToro, Phys. Rep. **410**, 335 (2005).
[23] V. Baran, M. Colonna, M. Di Toro, V. Greco, M. Zielinska-Pfabe, and H. H. Wolter, Nucl. Phys. **A703**, 603 (2002).
[24] T. X. Liu *et al*., Phys. Rev. C **69**, 014603 (2004).
[25] M. B. Tsang *et al*., Phys. Rev. C **64**, 054615 (2001).
[26] M. B. Tsang, W. A. Friedman, C. K. Gelbke, W. G. Lynch, G. Verde, and H. Xu, Phys. Rev. Lett. **86**, 5023 (2001).
[27] W. P. Tan *et al*., Phys. Rev. C **64**, 051901(R) (2001).
[28] D. Lunney, J. M. Pearson, and C. Thibault, Rev. Mod. Phys. **75**, 1021 (2003).
[29] A. E. L. Dieperink, Y. Dewulf, D. Van Neck, M. Waroquier, and V. Rodin, Phys. Rev. C **68**, 064307 (2003).
[30] W. Zuo, I. Bombaci, and U. Lombardo, Phys. Rev. C **60**, 024605 (1999).
[31] M. Brack, C. Guet, and H. B. Hakansson, Phys. Rep. **123**, 276 (1985).
[32] J. M. Pearson and R. C. Nayak, Nucl. Phys. **A668**, 163 (2000).
[33] W. D. Myers and W. J. Swiatecki, Nucl. Phys. **81**, 1 (1966).
[34] K. Pomorski and J. Dudek, Phys. Rev. C **67**, 044316 (2003).
[35] B. Borderie *et al*., Phys. Rev. Lett. **86**, 3252 (2001).
[36] D. R. Bowman *et al*., Phys. Rev. Lett. **67**, 1527 (1991).
[37] M. D'Agostino *et al*., Phys. Lett. **B371**, 175 (1996).
[38] L. Beaulieu *et al*., Phys. Rev. Lett. **84**, 5971 (2000).
[39] W. P. Tan, S. R. Souza, R. J. Charity, R. Donangelo, W. G. Lynch, and M. B. Tsang, Phys. Rev. C **68**, 034609 (2003).
[40] H. Xi, W. G. Lynch, M. B. Tsang, W. A. Friedman, and D. Durand, Phys. Rev. C **59**, 1567 (1999).
[41] H. Xi, W. G. Lynch, M. B. Tsang, and W. A. Friedman, Phys. Rev. C **54**, R2163 (1996).
[42] H. Johnston *et al*., Phys. Rev. C **56**, 1972 (1997).
[43] B. A. Li, C. M. Ko, and Z. Ren, Phys. Rev. Lett. **78**, 1644 (1997).
[44] V. Baran *et al*., Nucl. Phys. **A703**, 603 (2002).
[45] S. J. Yennello *et al*., Phys. Lett. **B321**, 15 (1994).
[46] C. A. Ogilvie, D. A. Cebra, J. Clayton, S. Howden, J Karn, A. Vander Molen, G. D. Westfall, W. K. Wilson, and J. S. Winfield, Phys. Rev. C **40**, 654 (1989).
[47] S. J. Yennello *et al*., *Proceedings of the 10th Winter Workshop on Nuclear Dynamics, Snowbird* (1994) (World Scientific, Singapore, 1994).
[48] R. P. Schmitt *et al*., Nucl. Instrum. Methods A **354**, 487 (1995).
[49] A. R. Raduta, Eur. Phys. J. A **24**, 85 (2005).
[50] M. B. Tsang, W. A. Friedman, C. K. Gelbke, W. G. Lynch, G. Verde, and H. S. Xu, Phys. Rev. C **64**, 041603(R) (2001).
[51] S. Albergo *et al*., Nuovo Cimento A **89**, 1 (1985).
[52] W. P. Tan, S. R. Souza, R. J. Charity, R. Donangelo, W. G. Lynch, and M. B. Tsang, Phys. Rev. C **68**, 034609 (2003).
[53] J. P. Bondorf, A. S. Botvina, A. S. Iljinov, I. N. Mishustin, and K. Sneppen, Phys. Rep. **257**, 133 (1995).
[54] J. Randrup and S. Koonin, Nucl. Phys. **A356**, 223 (1981).
[55] A. S. Botvina, A. S. Iljinov, I. N. Mishustin, J. P. Bondorf, R. Donangelo, and K. Sneppen, Nucl. Phys. **A475**, 663 (1987).
[56] D. H. E. Gross *et al*., Rep. Progr. Phys. **53**, 605 (1990).
[57] D. H. E. Gross *et al*., Z. Phys. A **309**, 41 (1982).
[58] X. Z. Zhang, D. H. E. Gross, S. Xu, and Y. M. Zheng, Nucl. Phys. **A461**, 641 (1987).
[59] A. S. Botvina *et al*., Nucl. Phys. **A584**, 737 (1995).
[60] R. P. Scharenberg *et al*., Phys. Rev. C **64**, 054602 (2001).
[61] N. Bellaize *et al*., Nucl. Phys. **A709**, 367 (2002).
[62] S. P. Avdeyev *et al*., Nucl. Phys. **A709**, 392 (2002).
[63] J. Pochodzalla *et al*., Phys. Rev. Lett. **75**, 1040 (1995).
[64] M. D'Agostino *et al*., Nucl. Phys. **A650**, 329 (1999).
[65] D. Cussol *et al*., Nucl. Phys. **A561**, 298 (1993).
[66] A. S. Botvina and I. N. Mishustin, Phys. Rev. C **63**, 061601(R) (2001).
[67] N. Buyukcizmeci, R. Ogul, and A. S. Botvina, Eur. Phys. J. **25**, 57 (2005).